

Nickel Alloying Significantly Enhances the Power Density of Ruthenium-Based Supercapacitors

Ahiud Morag,^{*,[a, b]} Nitzan Shauloff,^[a, b] Nitzan Maman,^[b] Natalya Froumin,^[b]
Vladimir Ezersky,^[b] and Raz Jelinek^{*,[a, b]}

Supercapacitors operating at high frequencies while exhibiting high capacitance have been challenging to fabricate due to high resistance and constrained ion diffusion in the active layers. To overcome these limitations, thin layers of pseudocapacitive materials with high theoretical capacitance can be used. Still, construction of such electrodes exhibiting effective ion diffusion, sufficient electrochemically-active surface area, and high conductivity has encountered significant difficulties. Here, we integrated nickel atoms into a ruthenium layer through a simple electrochemical deposition method, produc-

ing a thin electrode comprising hexagonal nickel ruthenium (NiRu) nanodendrites. Further oxidation of the NiRu alloy generated a thin surface layer of pseudocapacitive RuO₂ exhibiting significant areal capacitance. A symmetric device from two NiRu/RuO₂ electrodes displayed an energy density of 0.714 μWh cm⁻² with a remarkable power density of 1500 mW cm⁻², ~250 W cm⁻³ for a full device. The NiRu/RuO₂ supercapacitor outperforms commercial capacitors in both energy and power densities and may replace bulky capacitors in microelectronic devices.

1. Introduction

Supercapacitors (SCs) have attracted growing attention in energy storage applications, portable and wearable electronic devices, and flexible microelectronics.^[1,2] In particular, high-frequency alternate current (AC) filtering and high power pulses are considered as promising applications.^[3,4] Such SCs need to exhibit low resistance to enable high current densities, efficient ion diffusion for utilization of the active materials at high charge/discharge rates, and low dimensions suitable for integration in microelectronic devices.^[5-7] These challenges have been tackled by different strategies. Miller et. al. showed that vertically aligned graphene sheets can operate at frequencies exceeding 1 kHz, whereas commercial SCs are limited to < 1 Hz.^[8] Sheng and co-workers fabricated 50 μm-thick layers of electrochemically reduced graphene oxide (rGO) operating at high frequencies with capacitance values around 0.3 mF cm⁻² and currents of 100 mA cm⁻².^[9] To further increase the capacitance and facilitate efficient ion diffusion, a multistep synthesis strategy was applied by growing vertically aligned carbon nanotubes (CNTs) on a graphene-coated Ni substrate.^[10]

Motivated by these studies, research on SCs which can operate at high frequency/scan rates have mostly focused on devices based upon electric double-layer capacitor (EDLC) mechanisms. Materials such as onion-like carbon,^[11] mesoporous carbon,^[12-14] covalent organic frameworks,^[15] and exfoliated graphene,^[16] have been promoted as candidates for high-frequency EDLC-based supercapacitors. Yet, low material densities and reduced specific capacitance generally require high mass loading in such devices in order to achieve high capacitance.^[17] Furthermore, elaborate synthesis procedures have been developed to generate the required high surface areas facilitating effective ion diffusion at high-frequencies.^[10,18,19] However, as material loading increases, ion diffusion becomes less efficient, effectively limiting the use of EDLC-based materials in high-frequency SC applications.^[16]

Pseudocapacitive materials, such as MnO₂,^[20] RuO₂,^[21] metal-organic frameworks,^[22-24] and MXene^[25] exhibit high capacitance density making them promising candidates for high-frequency SCs. However, a prevailing assumption is that pseudocapacitive-based materials exhibit significant kinetic limitations due to the electrochemical redox reaction responsible for the energy storage mechanism.^[26] Recently, however, we and others have shown that varied pseudocapacitive-based materials can operate at high frequencies and that redox reaction dynamics do not hinder supercapacitor performance.^[27-29] Indeed, it has been demonstrated that the interface between the active material and current collector plays a significant role in ion diffusion and electronic transport, thereby affecting the electrochemical performance of the device.^[29-31] In particular, electrode structure and surface morphology have been shown to exhibit critical roles in shaping device properties. A recent study reported, for example, showed that a polymer/MXene film fabricated via filtration displayed a pronounced void structure. The effective

[a] Dr. A. Morag, N. Shauloff, Prof. R. Jelinek
Department of Chemistry
Ben-Gurion University
P.O.B 653 Beer-Sheva, Israel
E-mail: ahivd@post.bgu.ac.il
razj@bgu.ac.il

[b] Dr. A. Morag, N. Shauloff, Dr. N. Maman, Dr. N. Froumin, Dr. V. Ezersky,
Prof. R. Jelinek
Ilse Katz Institute for Nanoscale Science and Technology
Ben-Gurion university
P.O.B 653 Beer-Sheva, Israel

Supporting information for this article is available on the WWW under
<https://doi.org/10.1002/batt.202000110>

ion diffusion and high conductivity of MXene,^[32] enabled operation at high frequencies.^[27] Yet, increasing film thickness resulted in a pronounced decrease in electrochemical performance due to ineffective ion diffusion, at high loading, limiting its practical applicability.^[27]

Here, we report the fabrication of a new ultrathin (< 500 nm) nanostructured electrodes based upon a binary nickel-ruthenium alloy prepared via a simple electrodeposition/electrochemical oxidation procedure. Detailed spectroscopic and microscopic analyses reveal that the electrodes comprised of a thin layer of hexagonal NiRu alloy surface-coated with RuO₂, which can operate at current densities exceeding 2 A cm⁻². The NiRu/RuO₂ electrodes, deposited upon flexible commercially available nickel foil, were employed for construction of a symmetric supercapacitor exhibiting superior electrochemical properties. In particular, the device yielded remarkable capacitance of 0.80 mF cm⁻² at a scan rate of 1000 V s⁻¹, energy densities as high as 0.71 μWh cm⁻², and power densities of 1500 mW cm⁻².

2. Results and Discussion

2.1. Electrode Synthesis and Structural Characterization

The supercapacitor design presented here is based upon construction of high surface area nickel-ruthenium electrodes via a simple electrochemical deposition, facilitating rapid surface redox reactions, efficient ion diffusion and high electrical conductivity. Figure 1 depicts the synthesis scheme and microscopic analysis of the NiRu/RuO₂ electrode. The simple fabrication process is illustrated in Figure 1A. First, electrodeposition of a NiRu alloy was carried out on a thin nickel foil, using a mixture of 0.01 M NiSO₄ and 0.01 M of RuCl₃ in 1 M Na₂SO₄, and applying a high scan rate of 10 V s⁻¹ for 2500 cycles (Figure S1). Importantly, the electrochemical deposition process generated highly branched NiRu nanostructures. A subsequent oxidation step was carried out through the application of additional cyclic voltammetry (CV) cycles in a 1 M Na₂SO₄ solution, generating a layer of electrochemically active RuO₂ on the surface of the NiRu nanostructures (Figure S2). The scanning electron microscopy (SEM) image in Figure 1A (see also Figure S3) depicts the electrode protruding NiRu/RuO₂ nanostructures.

Scanning transmission electron microscopy (STEM) images of the film cross-section in Figure 1B–C illuminate the remarkable dendritic morphology of the electrodeposited NiRu film. Importantly, the dendritic pattern, which has not been previously reported for nickel or ruthenium alloys, endows high electroactive surface area, significantly more extensive compared to electrodes prepared through electrodeposition of *only* ruthenium upon nickel foil.^[29] Accordingly, the STEM images in Figure 1B–C underscore the important contribution of the nickel constituent in the Ni/Ru parent solution to the structural and electrochemical properties of the electrode. Notably, the STEM images and electron dispersion spectroscopy (EDS) elemental maps in Figure 1B–C indicate that the final electro-

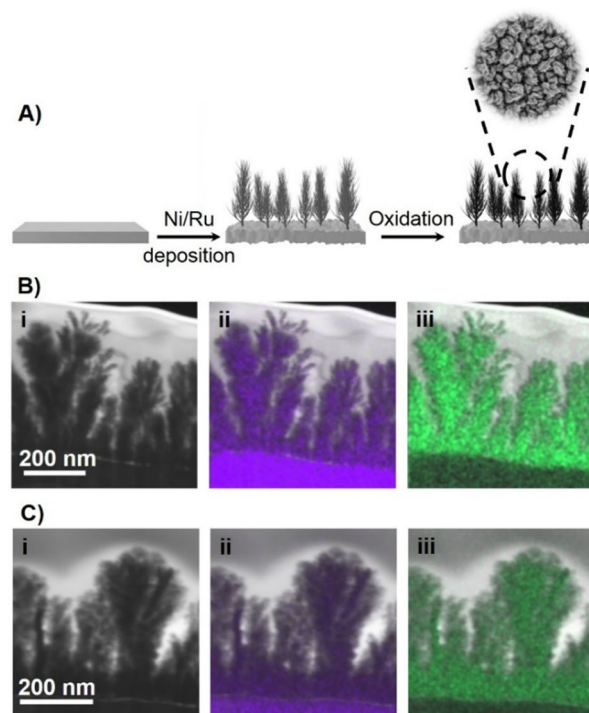


Figure 1. Preparation and morphology of the NiRu/RuO₂ electrode. A) Synthesis scheme for fabrication of the NiRu/RuO₂ layer upon Ni foil. The initial electrochemical deposition of NiRu alloy is followed by electrochemical oxidation of Ru into RuO₂. The inset shows a scanning electron microscopy (SEM) of the electrode surface. B–C) Cross-section scanning transmission electron microscopy (STEM) images (i), and EDS maps of Ni (ii) and Ru (iii) for the NiRu electrode (B) and NiRu/RuO₂ (C) electrode.

chemical oxidation step did not disrupt the dendritic film morphology, nor modified the uniform distribution of the nickel and ruthenium within the protruding nanostructures.

X-ray photoelectron spectroscopy (XPS) and high-resolution transmission electron microscopy (HRTEM) experiments presented in Figure 2 provide detailed information upon the atomic and crystalline organization of the NiRu alloy film. The Ru 3d core level binding energies of the pre-oxidized film reveal that almost 70% of the ruthenium at the electrode surface was already oxidized even before the electrochemical oxidation step (peaks at 280.73 eV and 281.64 eV in Figure 2A top spectrum corresponding to RuO₂ and RuO₂·xH₂O, respectively). Indeed, Ru(0) comprised only 30% of ruthenium at the electrode surface (Figure 2A, upper spectrum), and was further reduced to around 15% following electrochemical oxidation (Figure 2A, bottom spectrum).

Notably, the XPS data recorded for the oxidized film (Figure 2A, bottom spectrum) reveal that most of the RuO₂ on the surface was anhydrous (67%, peak at 280.73 eV), with a smaller percentage of hydrous RuO₂·xH₂O (16%, peak at 281.64 eV). This result is important since anhydrous RuO₂ exhibits higher electric conductivity compared to the hydrous phase, while RuO₂·xH₂O is known to contribute to diffusion-controlled processes.^[33] The X-ray diffraction (XRD) pattern in Figure S4 indicates formation of hexagonal NiRu layer in which the peaks corresponding to metallic Ni originate from the Ni

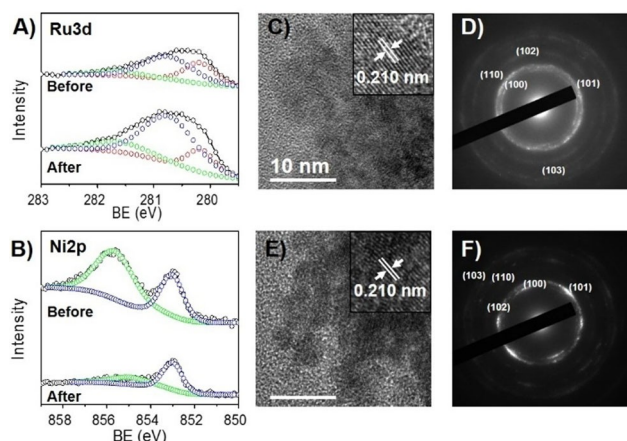


Figure 2. Characterization of NiRu and NiRu/RuO₂ electrodes. A) X-ray photoelectron spectra (XPS) of the ruthenium 3d core level before and after electrochemical oxidation. B) XPS of Ni 2p core levels before and after electrochemical oxidation. C) High-resolution transmission electron microscopy (HRTEM) image of the NiRu layer. The inset shows the d spacing of 0.210 nm corresponding to NiRu (002) plane. D) Selected area electron diffraction (SAED) of the NiRu layer and the corresponding crystal planes. E) HRTEM image of the NiRu/RuO₂ layer. The inset shows the d spacing of 0.210 nm corresponding to NiRu (002) plane. F) SAED of the NiRu/RuO₂ layer and the corresponding NiRu planes.

substrate, and, importantly, the RuO₂ layer was due to oxidation of Ru at the NiRu phase, rather than pure Ru (which was not detected in the XRD experiment).

XPS analysis of the Ni 2p core-level binding energies in Figure 2B complements the ruthenium XPS data (i.e. Figure 2A) and illuminates the organization of the nickel units in the electrodeposited film. Specifically, the XPS of as-deposited NiRu film (prior to electrochemical oxidation, Figure 2B, top spectrum) features a high-intensity satellite peak in 855.7 eV corresponding to NiO.^[34] Formation of NiO in the low potential region of the CV cycles was previously reported,^[35,36] confirming that the growth of a NiO layer occurred during the electrochemical deposition process. EDS analysis in Figure S5 and Table S1 indicates a relatively constant atomic ratio of 5:3:2 (Ni:Ru:O) throughout the film area, consistent with the formation of NiO (thereby increasing the relative abundance of nickel and oxygen). Notably, after the final electrochemical oxidation step (i.e., scheme in Figure 1A), the XPS peak ascribed to NiO disappeared, likely due to dissolution, and two peaks at 855.1 eV and 853.0 eV, corresponding to Ni in NiRu alloy, became the prominent spectral features.^[34] In addition, EDS analysis shows that the atomic ratio between the Ni and Ru changed to 4:5 (Ni:Ru; Figure S6 and Table S2). The disappearance of the NiO likely accounts to formation of Ni(OH)₂ which is dissolved in the solution.^[35]

HRTEM and diffraction analyses of the NiRu alloy film before (Figure 2C–D) and after electrochemical oxidation (Figure 2E–F) were carried out using cross-section lamella extracted by a focus ion beam (FIB). The HRTEM image of the as-deposited NiRu film in Figure 2C shows ubiquitous crystalline NiRu nanoparticles, while the amorphous RuO₂ is mainly localized on the film surface. The lattice spacing of 0.210 nm (Figure 2C, inset) corresponds to the (002) crystal plane of hexagonal NiRu (PDF

card No. 01-072-2536). This interpretation is further supported by the selected area electron diffraction (SAED) pattern in Figure 2D, displaying the (100), (101), (110), (102), and (103) crystal planes of hexagonal NiRu (PDF card No. 01-072-2536). Importantly, no crystalline RuO₂ peaks observed, furnishing additional evidence that the produced RuO₂ is amorphous. The SAED pattern further indicates that the deposited NiRu film does not contain metallic nickel. Together, the HRTEM and SAED analyses demonstrate that even after electrochemical oxidation, the nanostructures still comprise of hexagonal NiRu (Figure 2E–F). Interestingly, a close inspection of NiRu particles indicates the existence of small amounts of nickel-rich cubic NiRu phase (Figure S7).

2.2. Electrochemical Properties of a Symmetric NiRu/RuO₂ Supercapacitor

To evaluate the electrochemical performance of the NiRu/RuO₂ electrode we constructed symmetric supercapacitor devices comprising two NiRu/RuO₂ electrodes separated with a polystyrene mesh soaked with 1 M Na₂SO₄ solution (Figures 3–5). The optimal 0.01 M concentrations of both NiSO₄ and RuCl₃ were first determined through application of CV (Figure S8). Figure 3 depicts CV curves recorded at scan rates between 10–2000 V s⁻¹ for a symmetric device constructed from two NiRu/RuO₂ electrodes prepared according to this reagent ratio.

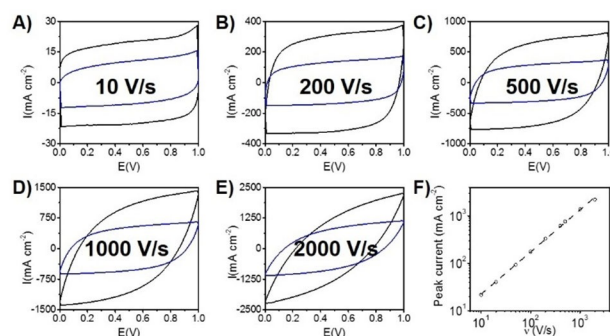


Figure 3. Electrochemical performance. Cyclic voltammetry (CV) curves of symmetric Ru/RuO₂ device (blue) and NiRu/RuO₂ device (black) at scan rates of 10 V s⁻¹ (A), 200 V s⁻¹ (B), 500 V s⁻¹ (C), 1000 V s⁻¹ (D), and 2000 V s⁻¹ (E). F) Peak current as a function of scan rate recorded for the NiRu/RuO₂ device, showing a near-linear behavior up to a scan rate of 2000 V s⁻¹.

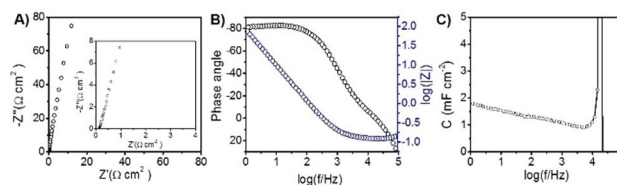


Figure 4. Electrochemical impedance spectroscopy. A) Nyquist plot in a frequency range of 100 kHz–1 Hz. The inset shows a magnification of the high-frequency region. B) Phase angle (black circles) and the log of the impedance (blue circles) as a function of the frequency (in a logarithmic scale). C) capacitance calculated from the imaginary part of the impedance as a function of frequency (in a logarithmic scale).

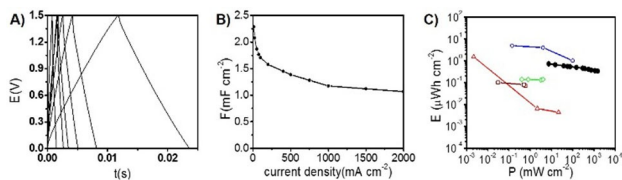


Figure 5. Galvanostatic charge/discharge analysis. A) Galvanostatic charge/discharge (GCD) curves at a voltage window of 1.5 V and current densities of 200 mA cm⁻², 500 mA cm⁻², 750 mA cm⁻², 1000 mA cm⁻², and 2000 mA cm⁻². B) Capacitance as a function of current density, calculated from the GCD curves. C) Ragone plot, presenting a comparison between current work (black circles) and devices comprising vertically aligned CNTs (blue circles),^[10] MoSe₂ (red triangles),^[46] MXene/polymer (green diamonds),^[27] and covalent organic framework (brown squares).^[15]

Importantly, the CV data in Figure 3 demonstrate excellent capacitor profiles of the NiRu/RuO₂ device even in high scan rates, displaying almost fully rectangular shapes up to 500 V s⁻¹ and a semi-rectangular CV curve shape at 1000 V s⁻¹. While no rectangular shape was recorded at 2000 V s⁻¹, likely due to potential losses at this high current density,^[37] this scan rate still yielded an excellent peak current (Figure 3F).

Notably, the current densities measured for the NiRu/RuO₂ supercapacitor in all scan rates (Figure 3, black curves) were profoundly higher (more than double) than the corresponding CV curves recorded for a device assembled from electrodes comprising just ruthenium deposited on the Ni foil (Figure 3, blue curves). The areal current density of 2200 mA cm⁻², recorded in the 2000 V s⁻¹ CV experiment (Figure 3E), is the highest areal current density achieved, for the best of our knowledge, for such a thin layer ultrahigh power density supercapacitors.^[38,39] Indeed, the current densities and capacitance properties manifested in the CV curves are significantly better than comparable electrochemical devices based on carbon nanotube (CNT),^[31] graphene,^[39] and pseudocapacitive materials including MXene-based devices.^[27] A previous report suggests that RuO₂ can undergo a redox reaction in a non-acidic environment according to Equation (1):^[40]

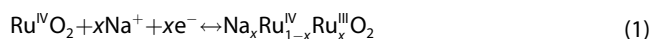


Figure 3F depicts the discharge peak current density as a function of the scan rate, showing a linear behavior nearly up to 2000 V s⁻¹, which is higher than previously reported RuO₂ devices,^[41] MXene devices^[27,28] and carbon-based devices.^[10,13,19] A high capacitance of 1.93 mF cm⁻² at 10 V s⁻¹, 0.79 mF cm⁻² at 1000 V s⁻¹ (41 % retention), and 0.46 mF cm⁻² at 2000 V s⁻¹ (24 % retention), calculated from the CV curves (Figure S9), far exceed corresponding values reported for other ultrahigh power supercapacitors.^[13,19,27] The important contribution of the nickel constituent to the remarkable electrochemical performance of the NiRu/RuO₂ device (e.g. Figure 3), both as enhancer of the porous morphology and vehicle for greater conductivity, is further supported by the observation of a highly limited capacitive properties of a Ni-only device (Figure S10).

Figure 4 presents the frequency response of the symmetric NiRu/RuO₂ device, calculated through application of electro-

chemical impedance spectroscopy. The Nyquist plot in Figure 4A shows a near perpendicular increase without any visible semicircular appearance, allowing modeling the device as a resistor and an ideal capacitor connected in series.^[8] The resistance at 120 Hz of NiRu/RuO₂ device, extracted from the Nyquist plot in Figure 4A, is 0.260 Ω cm², which is lower than previously reported planar devices comprising graphene,^[16] carbon nanotubes,^[10,31] and electrodeposited RuO₂,^[41] and comparable to mesoporous carbon devices fabricated on 3D templates.^[13]

The capacitive behavior of the NiRu/RuO₂ symmetric supercapacitor was further assessed by calculating the phase angle as a function of frequency (Figure 4B, black circles). In such measurements, a phase angle of -90° corresponds to ideal capacitive behavior, while a phase angle of 0° is indicative of a resistor.^[42] Notably, the calculated phase angle of -76° at 120 Hz is higher than angles reported for varied high capacitance devices, constructed from CNTs,^[31] graphene,^[39] reduced graphene oxide (rGO),^[9] MXene,^[27] and Ru/RuO₂.^[29] Notably, Figure 4B shows that a phase angle of -45°, which indicates an equal capacitor and resistor behavior, was attained at a frequency of 966 Hz, underscoring an exceptionally high frequency in which the device can still operate. The impedance as a function of the frequency, calculated from both the imaginary and real impedance components, is presented in Figure 4B (blue circles). The equivalent series resistance (ESR) of the NiRu/RuO₂ device, extracted from the impedance graph (Figure 4B, blue circles), is 0.122 Ω cm². Such a low value is important for high power density applications,^[43] and is lower than other pseudocapacitive devices prepared through elaborate methods.^[27,41]

Figure 4C depicts the areal capacitance, calculated from the imaginary component of the impedance as a function of frequency (see Supporting Information for detailed explanation). Echoing the superior electrochemical properties highlighted in Figures 3 and 4A–B, the high capacitance at 120 Hz (1.31 mF cm⁻²) outperforms devices fabricated by varied other methods, including vertically aligned graphene on cellulose fibers,^[39] vertically aligned CNTs,^[10] MXene,^[27] and other carbon-based materials.^[13,19,44] This result is likely due to the high surface area afforded by the NiRu nanostructures. From the calculated capacitance and resistance at 120 Hz, a very low RC time constant (τ_{RC}) of 0.31 ms was obtained. Notably, while high capacitance generally gives rise to an increase in τ_{RC} , the value obtained for the new NiRu/RuO₂ device is significantly lower than many published devices.^[10,13] Table S3 summarizes the electrochemical parameters obtained in the current work compared to varied other state-of-the-art devices, underscoring the superior capacitance performance achieved here, using a simple electrochemical deposition process compared to elaborated steps required in EDLC-based SCs.

The energy and power storage properties of the NiRu/RuO₂ supercapacitor were evaluated using galvanostatic charge/discharge (GCD) at a high voltage window of 1.5 V (Figure 5).^[43,45] Notably, no water decomposition was observed even at currents densities as low as 10 mA cm⁻² (Figure S11). Importantly, Figure 5A demonstrates that the device exhibited

excellent capacitor behavior, accounting for the linear response of the voltage and the low IR-drop (0.06 V at 200 mA cm⁻²), even in current densities up to 2000 mA cm⁻², which is among the highest areal current densities reported for such thin layers.^[10,15,27,46] This areal current density also corresponds to a high volumetric current density of more than 300 A cm⁻³ for the entire device, including the current collector and spacer, which is significantly higher than commercial capacitors. Indeed, considering that the thickness of the active layer is less than 2% of the overall volume of the device, the volumetric current density may be easily further increased upon reducing the thickness of the Ni current collector (currently 20 μm).

The areal capacitance graph in Figure 5B, calculated from the GCD curves, reveals high capacitance of 2.29 mF cm⁻² at 10 mA cm⁻² and 1.07 mF cm⁻² at 2000 mA cm⁻², accounting for almost 50% capacitance retention. Excellent cycle stability of 98.7% capacitance retention after 1 million cycles was also attained in the new device (Figure S12). These values outperform varied reported carbon-based electrodes,^[10,31,39] and further highlight the advantage of using pseudocapacitive-based materials.^[17] The Ragone plot in Figure 5C underscores the superior energy and power densities of the NiRu/RuO₂ supercapacitor compared to other reported devices. In particular, Figure 5C demonstrates that the symmetric NiRu/RuO₂ device can operate in significantly higher power densities compared to EDLC-based SCs, with a maximum energy density of 0.714 μWh cm⁻² (> 119 μWh cm⁻³) and maximum power density of 1500 mW cm⁻² (> 250 W cm⁻³). This remarkable feature of the NiRu/RuO₂ system likely corresponds to the high surface area of the NiRu nanostructures, furnishing high conductivity, efficient ion diffusion, and occurrence of rapid reversible redox reactions at the electrode surface.

3. Conclusions

We report fabrication of new pseudocapacitive supercapacitor electrodes comprising high surface area nickel-ruthenium alloy, which display exceptional electrochemical properties. The electrodes were prepared via a simple electrodeposition/electrochemical oxidation scheme, significantly easier to carry out than the elaborate synthesis steps required for construction of most current carbon-based ultrahigh power density supercapacitor devices. Notably, the synthesis scheme yielded a hexagonal ruthenium-rich NiRu nanostructured film coated with a thin layer of pseudocapacitive RuO₂, exhibiting core contributions to the electrochemical performance. In particular, the effective interface between RuO₂ coating and conductive NiRu nanostructures, further aided reduction of the overall device resistance. Furthermore, the inclusion of nickel in electrode composition played an important role in generation of the dendritic nanostructures and concomitant extensive surface area.

We employed the NiRu/RuO₂ electrodes to fabricate a symmetric supercapacitor displaying superior performance. Specifically, the device featured a phase angle of -76° at 120 Hz and ESR of 0.122 Ω cm², reflecting excellent ion and

electron transport properties essential for high frequencies and high current densities. The high areal capacitance of 1.07 mF cm⁻², achieved at a current density of 2000 mA cm⁻² (> 300 A cm⁻³ for a full device), underscores the excellent electrochemical properties and potential of the pseudocapacitive NiRu/RuO₂ system compared to both EDLC-based supercapacitors as well as other reported two-dimensional pseudocapacitive-based materials. Indeed, the high current densities we accomplish with the new NiRu/RuO₂ device attest to the fact that the electrode materials could successfully overcome currently encountered conductivity and diffusion barriers in other systems.

In conclusion, this study introduces a new electrode construct for ultrahigh power supercapacitors, which could be readily employed in varied applications, including wearable and portable microelectronics. We believe that the NiRu alloy system could be a model for the growth of other high surface area pseudocapacitive-based materials. Such composites may overcome disadvantages in current supercapacitor technologies such as low conductivity of transition metal oxides and slow diffusion kinetics in electrodeposited layers.

Experimental Section

Materials

Ni foil, 30 μm thick, was purchased from MTI corporation. RuCl₃ hydrate (40–43% Ru) and NiSO₄·7H₂O (99%) were purchased from STREM chemicals. Polystyrene (Mw ~ 280 kDa) was purchased from Sigma Aldrich. Dimethylformamide was purchased from J. T. Baker, and Na₂SO₄ (anhydrous 99%) was purchased from Loba Chemie. All chemicals were used as received. The water used in the experiments were doubly purified by a Barnstead D7382 water purification system (Barnstead Thermolyne, Dubuque, IA), at 18.2 MΩ cm resistivity.

Electrode fabrication

Deposition of Ni, Ru and NiRu was carried out on a commercial Ni foil. A 1 M Na₂SO₄ deposition solution contained RuCl₃ (0.000–0.015 M) and NiSO₄·7H₂O (0.000–0.0015 M) was used. The deposition was conducted using a 3-electrodes configuration with the Ni foil as the working electrode, Pt wire as the counter electrode and Ag|AgCl (3 M KCl) as the reference electrode. The deposition was achieved using cyclic voltammetry (CV) cycles between 0 V and -1.1 V vs reference electrode at a scan rate of 10 V s⁻¹. The deposition of either Ni, Ru or NiRu was achieved using different precursors concentration at 2.5k cycles. Subsequent oxidation of the Ru to RuO₂ was carried out by running 5k CV cycles at a scan rate of 10 V s⁻¹ in a voltage window of 0 and 0.8 V using a 3-electrodes configuration with either Ni/Ru or Ni/NiRu as the working electrode, Pt wire as the counter electrode and Ag|AgCl (3 M KCl) as the reference electrode in 1 M Na₂SO₄ solution. The deposition/oxidation was conducted on a SP-150 Bio-Logic (Claix, France).

Spacer fabrication

Polystyrene (PS) fibers were electrospun from a polystyrene solution in dimethylformamide (30% w/v), on 2.5 cm × 7.5 cm glass

for 40 min (under a 20 kV voltage with a 22 cm between needle and collector) and were annealed at 100 °C for 15 min. Following the annealing, carboxylation of the PS microfibers was carried out by exposing the PS fibers to air plasma for 2 min under vacuum at 85 W. Finally, the film was kept in a solution of 1 M Na₂SO₄ prior to use.

Device fabrication

Symmetric supercapacitors were composed of either 2 Ni/NiRu/RuO₂, Ni/Ru/RuO₂ or Ni/Ni electrodes exhibiting the same area and the PS spacer soaked in 1 M Na₂SO₄ solution. The devices were then wrapped with scotch tape.

Characterization

X-ray photoelectron spectroscopy (XPS) analysis was carried out using Thermo Fisher ESCALAB 250 instrument (England) with a basic pressure of 2×10^{-9} mbar. The samples were irradiated in two different areas using monochromatic Al K α 1486.6 eV X-rays, using a beam size of 500 μ m. The high energy resolution measurements were performed with a pass energy of 20 eV. The core level binding energies of the Ru 3d and Ni 2p peaks were normalized by setting the binding energy for the C1s at 284.8 eV. **High resolution transmission electron microscopy (HRTEM)** images were recorded on a 200 kV JEOL JEM-2100F (Tokyo, Japan). **Scanning electron microscopy (SEM)** images were recorded on Verios 460 L FEI (Czech Republic). **X-ray diffraction (XRD)** data was obtained using Panalytical Empyrean powder diffractometer (PANalytical, Almelo, Netherlands) equipped with a parabolic mirror on incident beam providing quasi-monochromatic Cu K α radiation ($\lambda = 1.54059$ Å) and X'celerator linear detector. Data were collected in the grazing geometry with constant incident beam angle equal to 1° in a 2 θ range of 30–80° with a step equal to 0.05°. **Scanning transmission electron microscopy (STEM)** images were recorded on a Helios G4 UC instrument and **electron dispersion spectroscopy (EDS)** map was measured on the same tool with silicon drift X ray detector (Brooker Xflash60) for 5 min at 15 kV and current of 1.6 nA.

Lamellas for cross section TEM imaging were fabricated using a Helios G4 UC dual beam **focus ion beam (FIB)/SEM** (Thermo Fisher Scientific). The sample was covered with 0.5 μ m of carbon using electron deposition followed by another 1 μ m of carbon ion deposition. Next, Ga ion beam was used to mill around the protective layer and an Easylift (Thermo Fisher Scientific) micro-manipulator was used to lift out the lamella from the bulk and attached it to a TEM grid. Further reduction of thickness and cleaning of the lamella was done with 30 kV Ga ion beam probe from both sides to a thickness of ~150 nm and then with 5 kV probe until the thickness was around 50 nm.

Electrochemical measurements: cyclic voltammetry (CV) was conducted in voltage ranges between 0–1 V. **Galvanostatic charge/discharge** measurements were conducted at current density in the range of 10–2000 mA cm⁻² in a voltage window of 1.5 V. **Electrochemical impedance measurements** were conducted between 1 Hz – 100 kHz with a sinus amplitude of 5 mV. Cycle stability measurements were conducted in a scan rate of 10 V s⁻¹ in a voltage window of 0–1 V for 1 million cycles. The electrochemical measurements were conducted in 2 electrodes configuration on either a CH instrument 760 C (Austin, TX) or a Bio-Logic SP-150 (Claix, France).

Acknowledgements

We are grateful to the Israeli Innovation Authority for generous support under the “Kamin” Program. The authors wish to thank Roxana Golan for the SEM measurements and Dr. Dimitry Mogiliansky for the XRD measurements.

Conflict of Interest

The authors declare no conflict of interest.

Keywords: alloys · energy storage · RuO₂ · pseudocapacitor · areal capacitance

- [1] J. Wang, F. Li, F. Zhu, O. G. Schmidt, *Small Methods* **2018**, 1800367, 1800367.
- [2] M. Beidaghi, Y. Gogotsi, *Energy Environ. Sci.* **2014**, 7, 867.
- [3] J. R. Miller, R. A. Outlaw, B. C. Holloway, *Electrochim. Acta* **2011**, 56, 10443–10449.
- [4] R. Dougal, I. G. Brown, S. K. Händel, in *Handb. Vac. Arc Sci. Technol.*, Elsevier, **1996**, pp. 625–699.
- [5] K. Jiang, Q. Weng, *ChemSusChem* **2020**, 13, 1420–1446.
- [6] H. Li, Q. Zhao, W. Wang, H. Dong, D. Xu, G. Zou, H. Duan, D. Yu, *Nano Lett.* **2013**, 13, 1271–1277.
- [7] B. Xie, Y. Wang, W. Lai, W. Lin, Z. Lin, Z. Zhang, P. Zou, Y. Xu, S. Zhou, C. Yang, et al., *Nano Energy* **2016**, 26, 276–285.
- [8] J. R. Miller, R. A. Outlaw, B. C. Holloway, *Science* **2010**, 329, 1637–1639.
- [9] K. Sheng, Y. Sun, C. Li, W. Yuan, G. Shi, *Sci. Rep.* **2012**, 2, 247.
- [10] J. Lin, C. Zhang, Z. Yan, Y. Zhu, Z. Peng, R. H. Hauge, D. Natelson, J. M. Tour, *Nano Lett.* **2013**, 13, 72–78.
- [11] D. Pech, M. Brunet, H. Durou, P. Huang, V. Mochalin, Y. Gogotsi, P.-L. L. Taberna, P. Simon, *Nat. Nanotechnol.* **2010**, 5, 651–654.
- [12] M. Zhao, J. Nie, H. Li, M. Xia, M. Liu, Z. Zhang, X. Liang, R. Qi, Z. L. Wang, X. Lu, *Nano Energy* **2019**, 55, 447–453.
- [13] N. Ji, J. Park, W. Kim, *ACS Omega* **2019**, 4, 18900–18907.
- [14] J. Joseph, A. Paravannoor, S. V. Nair, Z. J. Han, K. Ostrikov, A. Balakrishnan, K. (Ken) Ostrikov, A. Balakrishnan, *J. Mater. Chem. A* **2015**, 3, 14105–14108.
- [15] Y. Yusran, H. Li, X. Guan, D. Li, L. Tang, M. Xue, Z. Zhuang, Y. Yan, V. Valtchev, S. Qiu, et al., *Adv. Mater.* **2020**, 32, 1907289.
- [16] Z.-S. Wu, Z. Liu, K. Parvez, X. Feng, K. Müllen, *Adv. Mater.* **2015**, 27, 3669–3675.
- [17] P. Yang, W. Mai, *Nano Energy* **2014**, 8, 274–290.
- [18] A. Porkovich, Z. Ziadi, P. Kumar, J. Kioseoglou, N. Jian, L. Weng, S. Steinhauer, J. Vernieres, P. Grammatikopoulos, M. Sowwan, *ACS Nano* **2019**, 13, 12425–12437.
- [19] D. Zhao, W. Chang, C. Lu, C. Yang, K. Jiang, X. Chang, H. Lin, F. Zhang, S. Han, Z. Hou, et al., *Small* **2019**, 15, 1901494.
- [20] A. Morag, J. Y. Becker, R. Jelinek, *ChemSusChem* **2017**, 10, 2736–2741.
- [21] A. Ferris, S. Garbarino, D. Guay, D. Pech, *Adv. Mater.* **2015**, 27, 6625–6629.
- [22] Z. Liang, R. Zhao, T. Qiu, R. Zou, Q. Xu, *EnergyChem* **2019**, 1, 100001.
- [23] X. Li, X. Yang, H. Xue, H. Pang, Q. Xu, *EnergyChem* **2020**, 2, 100027.
- [24] X. Xiao, L. Zou, H. Pang, Q. Xu, *Chem. Soc. Rev.* **2020**, 49, 301–331.
- [25] M. Naguib, V. N. Mochalin, M. W. Barsoum, Y. Gogotsi, *Adv. Mater.* **2014**, 26, 992–1005.
- [26] B. E. Conway, *J. Electrochem. Soc.* **1991**, 138, 1539.
- [27] G. S. Gund, J. H. Park, R. Harpalsinh, M. Kota, J. H. Shin, T. il Kim, Y. Gogotsi, H. S. Park, *Joule* **2019**, 3, 164–176.
- [28] Q. Jiang, N. Kurra, K. Maleski, Y. Lei, H. Liang, Y. Zhang, Y. Gogotsi, H. N. Alshareef, *Adv. Energy Mater.* **2019**, 1901061, 1901061.
- [29] A. Morag, N. Maman, N. Froumin, V. Ezersky, K. Rechav, R. Jelinek, *Adv. Electron. Mater.* **2020**, 6, 1900844.
- [30] P. Huang, M. Heon, D. Pech, M. Brunet, P. L. Taberna, Y. Gogotsi, S. Lofland, J. D. Hettinger, P. Simon, *J. Power Sources* **2013**, 225, 240–244.
- [31] Y. Rangom, X. (Shirley) Tang, L. F. Nazar, *ACS Nano* **2015**, 9, 7248–7255.
- [32] X. Zhao, H. Xu, Z. Hui, Y. Sun, C. Yu, J. Xue, R. Zhou, L. Wang, H. Dai, Y. Zhao, et al., *Small* **2019**, 15, 1–8.

- [33] W. Sugimoto, H. Iwata, K. Yokoshima, Y. Murakami, Y. Takasu, *J. Phys. Chem. B* **2005**, *109*, 7330–7338.
- [34] Z. F. Zhao, Z. J. Wu, L. X. Zhou, M. H. Zhang, W. Li, K. Y. Tao, *Catal. Commun.* **2008**, *9*, 2191–2194.
- [35] M. S. Wu, C. H. Yang, M. J. Wang, *Electrochim. Acta* **2008**, *54*, 155–161.
- [36] S. J. Li, N. Xia, X. L. Lv, M. M. Zhao, B. Q. Yuan, H. Pang, *Sens. Actuators B* **2014**, *190*, 809–817.
- [37] B. E. Conway, *Electrochemical Supercapacitors*, Springer US, Boston, MA, **1999**.
- [38] C. Xu, L. Jiang, X. Li, C. Li, C. Shao, P. Zuo, M. Liang, L. Qu, T. Cui, *Nano Energy* **2020**, *67*, 104260.
- [39] N. Islam, M. N. F. Hoque, W. Li, S. Wang, J. Warzywoda, Z. Fan, *Carbon* **2019**, *141*, 523–530.
- [40] B. Shen, X. Zhang, R. Guo, J. Lang, J. Chen, X. Yan, *J. Mater. Chem. A* **2016**, *4*, 8180–8189.
- [41] T. M. Dinh, K. Armstrong, D. Guay, D. Pech, *J. Mater. Chem. A* **2014**, *2*, 7170–7174.
- [42] A. Eftekhari, *J. Mater. Chem. A* **2018**, *6*, 2866–2876.
- [43] A. Ferris, B. Reig, A. Eddarir, J.-F. Pierson, S. Garbarino, D. Guay, D. Pech, *ACS Energy Lett.* **2017**, *2*, 1734–1739.
- [44] W.-H. Chiang, W. Kinzelbach, W.-H. Chiang, W. Kinzelbach, N. Islam, S. Li, G. Ren, Y. Zu, J. Warzywoda, S. Wang, et al., *Nano Energy* **2017**, *40*, 107–114.
- [45] H. Xia, Y. S. Meng, G. Yuan, C. Cui, L. Lu, *Electrochem. Solid-State Lett.* **2012**, *15*, A60.
- [46] Z. Jiang, Y. Wang, S. Yuan, L. Shi, N. Wang, J. Xiong, W. Lai, X. Wang, F. Kang, W. Lin, et al., *Adv. Funct. Mater.* **2018**, *1807116*, 1807116.

Manuscript received: May 18, 2020
Revised manuscript received: June 12, 2020
Accepted manuscript online: June 19, 2020
Version of record online: July 8, 2020